

# Fabrication and Characterization of an Integrated Microsystem for Protein Preconcentration and Sensing

Philip Dextras, Kristofor R. Payer, Thomas P. Burg, *Member, IEEE*, Wenjiang Shen, Ying-Chih Wang, Jongyoon Han, *Member, IEEE*, and Scott R. Manalis

**Abstract**—We report on a fabrication and packaging process for a microsystem consisting of a mass-based protein detector and a fully integrated preconcentrator. Preconcentration of protein is achieved by means of a nanofluidic concentrator (NC), which takes advantage of fast nonlinear electroosmotic flow near a nanochannel–microchannel junction to concentrate charged molecules inside a volume of fluid on the order of 1 pL. Detection of preconcentrated protein samples is accomplished by passing them through a suspended microchannel resonator (SMR), which is a hollow resonant cantilever serially connected to the NC on the same device. The transit of a preconcentrated sample produces a transient shift in the cantilever’s resonance frequency that is proportional to the density of the sample and, hence, the concentration of protein contained in it. A device containing both NC and SMR structures was produced using a novel fabrication process which simultaneously satisfies the separate packaging requirements of the two structures. The initial testing of this prototype device has demonstrated that the integrated SMR can accurately measure the concentration of a bovine serum albumin solution, that was preconcentrated using the integrated NC. Future improvements in the fabrication process will allow

site-specific surface modification of the device and compatibility with separation methods, which will create opportunities for its application to immunoassays and universal detection. [2010-0092]

**Index Terms**—Anodic bonding, glass frit bonding, ion concentration polarization, preconcentration, semiconductor device packaging, vacuum packaging, wafer scale integration.

## I. INTRODUCTION

RECENTLY, the Han research group has developed a microdevice which takes advantage of fast nonlinear electroosmotic flow (EOF) in the vicinity of a nanochannel–microchannel junction to preconcentrate charged molecules by a factor from  $10^4$ - to  $10^6$ -fold in less than an hour [1], [2]. This nanofluidic concentrator (NC) possesses several advantages over other biomolecular preconcentration techniques. Methods such as field-amplified sample stacking [3]–[6], isotachopheresis [7], and micellar electrokinetic sweeping [8]–[10] have buffering requirements which can interfere with downstream sample processing, making them difficult to integrate with detectors. Electrokinetic trapping techniques show promise as an efficient way to concentrate proteins, but the linearity and stability of these methods are a concern [11]–[13]. Chromatographic preconcentration techniques capture proteins by hydrophobic interaction and hence are biased toward large hydrophobic proteins and less sensitive to smaller or more hydrophilic molecules [14]–[16]. Membrane filter preconcentration is another example of a method which is biased toward larger molecules [17], [18]. Compared with these alternatives, the NC method of biomolecular preconcentration is the most favorable in terms of general applicability to a wide range of molecular species, ease of integration, and rate of preconcentration. The existing NC devices with integrated sensing capabilities rely on fluorescent labeling of the target analyte molecules for detection. This approach is not ideal because the conjugation of target proteins to dye molecules can modify their chemical properties, which can interfere with sensing methods that require selective capture of the target by probe molecules. In addition, because fluorescent detection is subject to photobleaching, autofluorescence of the sensing environment, and fluctuations in the excitation-source intensity, quantitative sensing often depends on the repeatability of calibration protocols.

These limitations can be overcome by integrating the NC with a suspended microchannel resonator (SMR) sensor, as shown in Fig. 1. The SMR is a resonant cantilever with a fluid-filled microchannel running through it. The resonance

Manuscript received April 7, 2010; revised September 26, 2010; accepted October 12, 2010. This work was supported by the National Cancer Institute Contract R01CA119402 and NIH Cell Decision Process Center P50-GM68762. Subject Editor A. J. Ricco.

P. Dextras was with the Department of Biological Engineering, Massachusetts Institute of Technology, Cambridge, MA 02139 USA. He is now with the Department of Applied Chemistry, The University of Tokyo, Tokyo 113-8656, Japan (e-mail: dextras@icl.t.u-tokyo.ac.jp).

K. R. Payer is with the Microsystems Technology Laboratories, Massachusetts Institute of Technology, Cambridge, MA 02139 USA (e-mail: kpayer@mit.edu).

T. P. Burg was with the Department of Biological Engineering, Massachusetts Institute of Technology, Cambridge, MA 02139 USA. He is now with the Max Planck Institute for Biophysical Chemistry, 37077 Goettingen, Germany (e-mail: tburg@mpibpc.mpg.de).

W. Shen is with Innovative Micro Technology, Inc., Santa Barbara, CA 93117 USA (e-mail: WShen@imtmems.com).

Y.-C. Wang was with the Department of Mechanical Engineering, Massachusetts Institute of Technology, Cambridge, MA 02139 USA. He is now with RheoSense, Inc., San Ramon, CA 94583 USA (e-mail: gilwang@gmail.com).

J. Han is with the Department of Biological Engineering and the Department of Electrical Engineering and Computer Science, Massachusetts Institute of Technology, Cambridge, MA 02139 USA (e-mail: jyhan@mit.edu).

S. R. Manalis is with the Department of Biological Engineering and the Department of Mechanical Engineering, Massachusetts Institute of Technology, Cambridge, MA 02139 USA (e-mail: srm@mit.edu).

Color versions of one or more of the figures in this paper are available online at <http://ieeexplore.ieee.org>.

This paper has supplementary downloadable material available at <http://ieeexplore.ieee.org>, which is provided by the authors. The material consists of a video of size 8.67 MB. The video can be viewed with Windows Media Player. Contact dextras@icl.t.u-tokyo.ac.jp for further questions about this work.

Digital Object Identifier 10.1109/JMEMS.2010.2093563

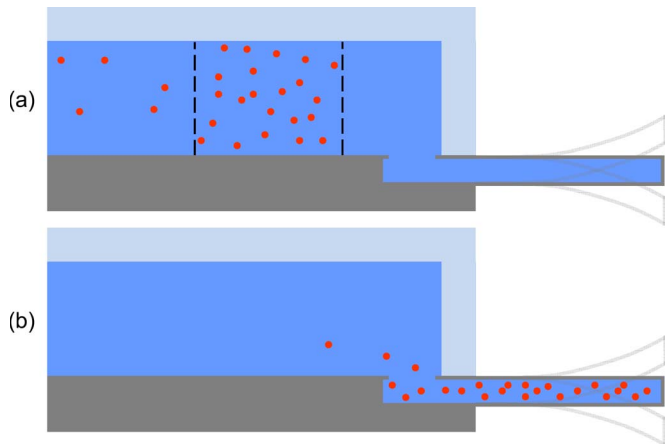


Fig. 1. Schematic cross section of the device showing (a) accumulation of analyte molecules inside the NC and (b) delivery of the preconcentrated analyte to the SMR sensor. The analyte increases the mass of the resonator, which causes a relative shift in its resonance frequency that is proportional to the analyte concentration.

frequency of the cantilever changes in proportion to the buoyant mass of molecules and ions added to the suspended microchannel, which makes it a general platform for quantitative label-free detection in fluid. For example, universal detection has been demonstrated by prefractionating mixtures by high-performance liquid chromatography and measuring the bulk density of the column's output on an SMR [19]. The SMR has also been used to conduct label-free immunoassays in blood serum by measuring the quantity of target protein captured by antibody probes attached to the surfaces of the suspended microchannel [20].

The sensitivity in both bulk density and surface-based detection with the SMR could be substantially enhanced by integrated preconcentration using an NC for sufficiently soluble protein analytes. In the case of surface-based assays, the benefit of preconcentration also depends on the dissociation constant ( $K_D$ ) of the probe system employed. Because of the small fixed volume ( $\sim 1$  pL) of concentrated samples produced by the NC, there exists a concentration below which the number of molecules contained in this volume will be less than the number of receptors on the surfaces of the SMR, resulting in sample depletion. Provided that  $K_D$  is larger than this threshold concentration divided by the maximum preconcentration factor achievable, the integrated system will achieve a greater equilibrium-bound fraction than would a flow-through system in which sample depletion is negligible. Since the present device has been demonstrated only for density-based measurement and not for surface-based measurement, design parameters were not optimized with respect to this threshold value of  $K_D$ , which was estimated to be 18 nM from simulations (see Appendix). In addition to improving the SMR sensitivity, integration may also provide benefits for the NC. The SMR's ability to measure the spatial and temporal dependences of ionic concentrations in the vicinity of the NC may provide new information about the underlying ion transport processes which could inform the design of future NC devices.

Here, we report a novel fabrication process which was used to produce a microsystem containing both NC and SMR

structures. A monolithic system is required in order to allow the minute sample volume from the preconcentrator to be transferred to the SMR without significant dispersion. The functionality of the integrated system has been demonstrated by preconcentrating a model aqueous protein solution using the NC, transferring the concentrated sample to the SMR, and measuring the final concentration obtained by SMR densitometry. By establishing successful operation of the NC and SMR simultaneously on the same device and efficient transfer of preconcentrated protein samples between them, an important first step has been undertaken in the development of highly sensitive universal detection systems and immunoassays.

## II. DESIGN

The integration of the NC and SMR was aided by the fact that the internal volume of existing stand-alone SMR devices ( $\sim 25$  pL) is comparable with the typical volume of concentrated protein samples which are produced in existing stand-alone NC devices ( $\sim 1$  pL), so that sample transfer and detection can be accomplished without significant dilution of the concentrated sample. Hence, the physical dimensions of the NC and SMR components of the integrated device were made as similar as possible to those of stand-alone devices which have been previously demonstrated [1], [21]. The integrated NC structure consists of two  $3\ \mu\text{m}$ -deep microchannels that are connected by a series of  $\sim 40$ -nm-deep nanochannels (Fig. 2). When these nanochannels are filled with media having an ionic strength of  $\sim 10$  mM, the Debye length is comparable with the nanochannel depth, which gives the nanochannel permselective ion transport properties when a longitudinal electric field  $E_n$  is applied. These nanochannels have silicon dioxide surfaces bearing negative fixed surface charges at near-neutral pH, and hence, positive counterions are transported more readily than negative coions. This results in the depletion of counterions from the anodic end of the nanochannel and enrichment at the cathodic end. To maintain charge neutrality, coion concentrations mirror these changes in counterion concentration, producing a depletion region of reduced ionic strength at the anodic end of the nanochannel, a condition which is referred to as ion concentration polarization [22]. If  $E_n$  is increased further, a situation may arise where the diffusion of counterions from the bulk will not be sufficient to maintain charge neutrality in the depletion region, in which case an extended space-charge layer (SCL) will form at the anodic end of the nanochannel. This layer can be thought of as an extension of the Debye layer of the nanochannel itself, with mobile counterions in the SCL screening the fixed charges that are present on the nanochannel walls. The concentration of counterions in the SCL, which is linearly dependent on the magnitude of  $E_n$ , gives rise to nonlinear electrokinetic phenomena when a tangential electric field  $E_t$  is applied longitudinally to the microchannel at the anodic end of the nanochannel. One of these phenomena is EOF of the second kind [23], [24], which is proportional to the product of  $E_n$  and  $E_t$  and is much stronger than the EOF observed ordinarily in microchannels, which scales simply as  $E_t$  [25]–[27]. Macromolecules are rapidly transported through

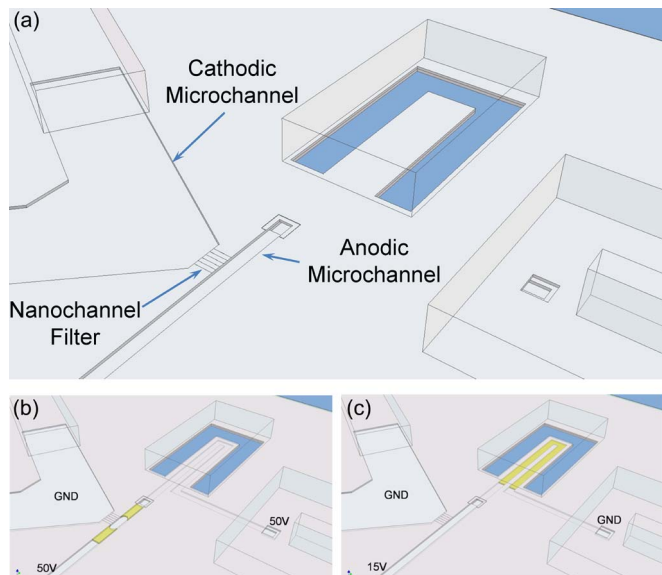


Fig. 2. (a) Computer-aided design drawing of the device showing the layout of channels used for preconcentration. (b) Preconcentration of protein is achieved by applying a potential across the nanochannel filter. In this drawing, the upper layer of the cantilever is made transparent to show the suspended microchannel running through it. (c) Preconcentrated protein is transferred to the sensor by EOF through the anodic microchannel.

the anodic microchannel by this nonlinear EOF, and those possessing fixed charges with their own associated Debye layers are repelled from the depletion region because the low ionic strength of this region makes it energetically unfavorable. This balance between strong EOF of the second kind and repulsion from the depletion region results in preconcentration of macromolecules at the outer boundary of the depletion region.

The main difference between the design of the integrated NC (Fig. 2) and that of the previous stand-alone NC devices [1] is the physical structure of the nanochannel filter. Although nanochannels in both cases were etched to the same depth of  $\sim 40$  nm, as determined by contact profilometry, differences in anodic bonding conditions between the two processes resulted in filters with higher ionic conductivities in the case of the integrated device. As a result, filters in the integrated device can support significant EOF with the application of a potential difference between the anodic and cathodic microchannels. This makes it possible to achieve self-stabilizing preconcentration with only one applied potential difference [Fig. 2(b)]. Once the desired target analyte concentration has been achieved, as determined by fluorescence imaging of dye molecules conjugated to the analyte, the normal electric field is removed, and a tangential electric field moves the concentrated analyte by EOF through the suspended microchannel of the SMR, which is serially connected to the anodic microchannel of the NC [Fig. 2(c)]. The transient shift in resonant frequency of the SMR corresponding to the transit of the concentrated analyte is proportional to its density and, hence, its concentration. This information, combined with the experimentally determined rate of preconcentration for a given analyte and the preconcentration time, provides a measure of the analyte's initial concentration.

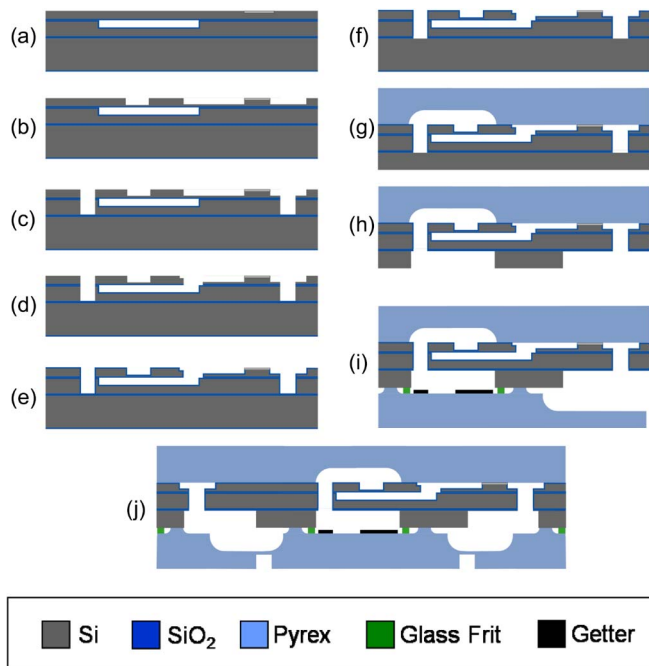


Fig. 3. Fabrication and packaging process for the device. (a) Nanochannels are etched into SOI substrates containing oxidized cavities. (b) RIE of NC channels and SMR windows. (c) DRIE of cantilever outlines and front side of ports. (d) SMR and NC anodic microchannels are connected by RIE. (e) Thermal oxidation. (f) Oxide is removed from the bottoms of SMR outlines/ports. (g) Anodic bonding to Pyrex lid and thinning of bulk silicon. (h) DRIE releases cantilevers and completes ports. (i) Glass-frit bonding to Pyrex base. (j) Partial diesaw cuts isolate the central island of Pyrex base used for vacuum packaging of resonators. Full-depth diesaw cuts define die edges. The outer pieces of Pyrex base are removed to expose ports.

### III. FABRICATION AND PACKAGING

A significant challenge in the integration of the fabrication processes for the stand-alone NC and SMR devices into a single process (Fig. 3) is the requirement that the glass lid of the device, which provides the upper surface of NC nanochannels, must not contain fluidic access holes. The reason for this is that empirical studies have established that the presence of such holes interferes with the anodic bonding of nanochannels in a way that is detrimental to the performance of the NC (see Appendix). Hence, the fluidic ports in stand-alone NC devices have previously been made through the silicon base of the device. On the other hand, the fluidic ports in stand-alone SMR devices have exclusively been located in the glass lid because the base of these devices contains glass frits which are required for vacuum packaging of the resonators and are compromised by contact with fluids [28]. Therefore, in order to accommodate the requirements of both the NC and SMR, a hybrid architecture was created in which part of the device's lower surface is used for fluidic ports, and the remainder is used for resonator vacuum packaging. In the completed integrated device [shown schematically in cross section in Fig. 3(j)], the upper part of the package is provided by a continuous anodically bonded glass lid. The lower part of the package is a discontinuous frit-bonded glass base which hermetically encloses the central portion of the device containing the resonator while leaving the fluid ports open to external interconnects from below.

The front-side processing of the device [Fig. 3(a)–(g)] was carried out in the Microsystems Technology Laboratories at the Massachusetts Institute of Technology. The starting substrates consisted of custom silicon-on-insulator (SOI) wafers (150-mm diameter and 675- $\mu\text{m}$  total thickness, Icemos Technology, Belfast, U.K.) containing 3- $\mu\text{m}$ -deep channels buried within a 10- $\mu\text{m}$ -thick silicon layer on top of a 2- $\mu\text{m}$ -thick silicon dioxide film [buried oxide (BOX)]. The buried channels define the suspended microchannel of the SMR, and their surfaces possess a 500-nm-thick thermally grown passivation oxide. Nanochannels were etched into the silicon using a reactive ion etch (RIE), and their depth was found to be 42–43 nm using a contact profilometer. The anodic and cathodic microchannels of the NC were defined by RIE, and the same etch was used to produce windows in the layer of silicon above the suspended microchannel in order to enable fluorescence imaging of the contents of this buried channel. Next, a series of deep RIEs (DRIEs) terminating on the BOX was used to define the outline of the cantilever and the front-side portion of the device's fluidic ports. In order to etch through the BOX film in the SOI device layer, the photolithographic pattern corresponding to these features was etched a total of three times using two alternating DRIE recipes, with one being selective to silicon and the other to silicon dioxide. The silicon and silicon dioxide in the region of overlap between the SMR and NC channels were removed by RIE, thus creating a connection between them. A 500-nm-thick wet thermal oxide was then grown on the wafers in order to electrically insulate all exposed silicon surfaces. The BOX layer was removed from the bottoms of the fluidic ports and the cantilever outlines by RIE. The SOI stack was then anodically bonded to 500- $\mu\text{m}$ -thick Pyrex wafers containing 50- $\mu\text{m}$ -deep fluid channels and resonator cavities which were etched in concentrated HF using a low-pressure chemical vapor deposition polysilicon mask. Anodic bonding conditions were empirically optimized together with the nanochannel dimensions in order to achieve the highest possible bond strength without collapse of the nanochannel (see Appendix). These studies showed that a filter consisting of three 5- $\mu\text{m}$ -wide nanochannels separated by 5- $\mu\text{m}$ -wide pillars was the most resistant to nanochannel collapse and that this structure could be bonded with either a steel or graphite chuck at 400 °C and 1 kV with less than 10% of the bonded filters on the wafer displaying collapsed nanochannels ( $n = 15$ ). This filter design was therefore employed in all integrated devices, and the wafer stacks were anodically bonded at 350 °C and 1 kV.

The backside processing of wafer stacks [Fig. 3(g)–(j)] was carried out by Innovative Micro Technology (Santa Barbara, CA). Using the anodically bonded glass lid as a handle, the bulk silicon of the wafer stack was thinned to  $\sim 100 \mu\text{m}$  by mechanical grinding and chemical–mechanical polishing. Cantilevers were released by a DRIE that is selective to silicon over silicon dioxide, which terminated on the BOX, and the same etch defined the bottom-side portion of the fluidic ports. The wafer stack was then hermetically packaged under vacuum conditions by glass-frit bonding to a 500- $\mu\text{m}$ -thick Pyrex wafer containing standoff structures to control the compression of the frits and getters for gas sequestration. To prepare the Pyrex base for glass-frit bonding, standoffs were etched with

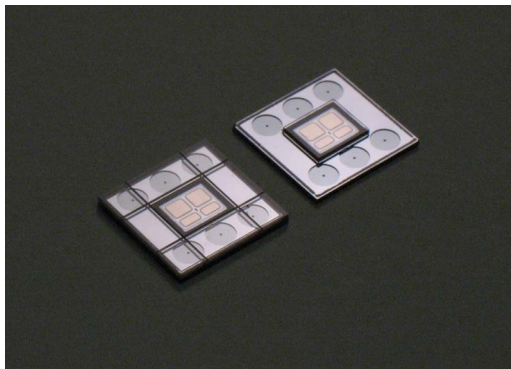


Fig. 4. Photographs of completed devices (left) before and (right) after the removal of the sacrificial Pyrex base material (scale bar: 1 cm).

HF, followed by silk screening of the glass frits and, finally, getter deposition. In order to enable the removal of Pyrex base material covering the fluidic ports while maintaining the integrity of the resonator packaging, a novel glass-frit design and diesawing scheme was developed. As shown in Fig. 3(j), each device possessed two continuous frits: an inner frit that encircled only the resonator and an outer frit that followed the perimeter of the die. Diesawing was carried out in two stages. First, partial-depth diesaw cuts were performed on the Pyrex base just outside the inner frits, leaving a rectangular island of Pyrex frit bonded to the central resonator region of each device and connected to the rest of the Pyrex base only by thin membranes. Next, full-depth diesaw cuts were performed just outside the outer frits, separating the dies. The function of the outer frit is to prevent liquid from the full-depth diesaw slurry from entering the fluid ports, potentially contaminating the device channels, or from attacking the inner frits needed for resonator packaging. After diesawing, the sacrificial outer frit was partially dissolved with acetone on individual devices to minimize the amount of mechanical force needed to separate the eight pieces of peripheral Pyrex base material from the central island, thus providing access to the device's fluid ports without damaging the vacuum-bearing inner frit. A photograph of the device before and after the removal of the peripheral Pyrex material is shown in Fig. 4.

#### IV. CHARACTERIZATION

To establish the functionality of the device, a solution of bovine serum albumin (BSA) conjugated to the fluorophore AlexaFluor 488 (Invitrogen, Carlsbad, CA) was concentrated using the NC while monitoring its concentration by fluorescence imaging. After 1 min of preconcentration, the concentrated protein was made to flow through the SMR while simultaneously monitoring the SMR's resonance frequency. The fluorescence of the preconcentrated sample just before the transfer to the SMR could then be compared with the transient SMR resonance frequency response during the sample transit in order to demonstrate the integrated SMR's ability to quantify the amount of protein contained in the preconcentrated sample.

Further characterization was inhibited by the fact that the integrated device packages were highly fragile compared with those of stand-alone devices, so that fluidic interconnects



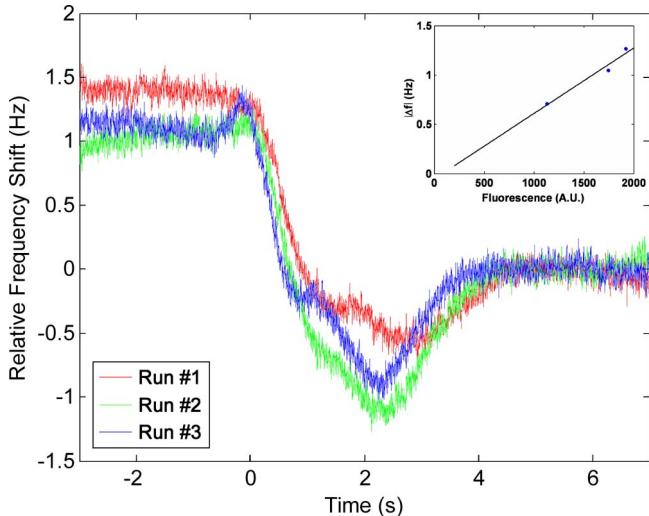


Fig. 7. SMR resonance-frequency time courses corresponding to three iterations of the experiment described in Fig. 6. The shift in resonance frequency corresponds temporally to the transit of protein through the SMR, as can be seen in the fluorescence image sequences. The concentration of protein is proportional in magnitude to the minimum value of the resonance frequency relative to its baseline immediately after the sample transit, this quantity is plotted against the mean fluorescent intensity of the sample just prior to the sample transit.

suspended portion of the anodic microchannel; therefore, samples can be transferred and detected before significant dilution takes place. The recorded SMR resonance-frequency time courses showed a transient decrease in the resonance frequency, which corresponds temporally to the transit of concentrated protein, as determined by the recorded sequences of fluorescence images (Fig. 7). The resonance frequency did not return to its original baseline until several seconds after the data shown in Fig. 7, which was attributed to the transit of buffer ions that were locally concentrated by the NC. Since the concentrated protein sample overlaps spatially with this region of increased ion concentration, the resonance frequency minimum was compared to its baseline value immediately after the transit of protein to determine the relative shift, which was solely due to the presence of protein. This quantity was found to be proportional to the measured fluorescence intensity of the protein sample just before it was transferred to the SMR (inset of Fig. 7), which indicates that the measured shift in resonance frequency is an accurate measure of protein concentration under these experimental conditions. The magnitude of this shift is also comparable to the previous BSA density measurements made with a stand-alone SMR device, where a frequency shift per unit density of  $1.7 \text{ Hz} \cdot (\text{g/L})^{-1}$  was observed [19]. In the experiments reported here, we measured a final concentration of  $1.4 \text{ g/L}$  after 1 min of preconcentration. This concentration is expected to produce a frequency shift of  $1.4 \text{ Hz}$  in the integrated system, using the sensitivity of the stand-alone SMR quoted earlier and correcting for differences in mass, resonance frequency, and internal volume. The discrepancy between this value and the measured average frequency shift of  $1.0 \pm 0.3 \text{ Hz}$  is most likely due to the diffusive dilution of the sample observed after preconcentration and the fact that the concentrated sample's volume is too small to fill the internal volume of the SMR.

## V. CONCLUSION

A device containing both NC and SMR structures has been fabricated using a novel packaging process, and the integrated SMR has been used to measure the concentration of a protein which was preconcentrated using the integrated NC. One obstacle that remains in the application of this device to quantitative label-free sensing of analytes is the variability in the rate of preconcentration observed with the integrated NC. This was attributed to differences in the structure of the integrated NC's nanochannel filter compared to that of stand-alone NC devices. Although the total cross section of nanochannels, as determined by profilometry before anodic bonding, was not significantly different between these two devices, the measured ionic conductivity was almost an order of magnitude larger in the case of the integrated device. This suggests partial delamination of the anodic bond, which may be due to changes in anodic bonding conditions related to the modified channel layout. Weaker anodic bonds in the integrated devices could also result from a reduced electric field at the bond interface during bonding due to the presence of an additional silicon dioxide film in the SOI substrate that was not present in substrates used to fabricate stand-alone NC devices. Another limitation of the increased filter conductivity of the integrated NC is the high EOF through the filter, which diminishes concentration polarization and causes the SCL to collapse against the filter for increasing values of  $E_n$ . Since this situation cannot be corrected by adding a tangential electric field, the preconcentration rate is proportional to  $E_n^2$ , and the collapse of the SCL represents a practical limitation on throughput. In contrast, stand-alone NC devices are able to support larger values of  $E_n$  by increasing  $E_t$ , and since the preconcentration rate is proportional to the product of the two electric fields in this mode of operation, a significantly higher throughput can be achieved. Future integrated device designs should therefore be informed by more extensive studies on the effects of local channel topography and substrate composition on the anodic bonding of nanochannels in order to achieve the desired filter conductivity. The realization of such a device will also make it possible to carry out preconcentration inside the SMR, which could open up new possibilities for studying the spatial and temporal variations in ionic concentrations resulting from preconcentration. In order to explore the applications in immunodetection and universal detection, improvements in the fabrication and packaging processes are needed to make integrated devices which are less fragile and, hence, compatible with pressurized fluid interconnects required for active pressure-driven flow control. This will enable both site-specific surface modifications, which are needed for surface immunoassays, and compatibility with separation methods.

## APPENDIX

### A. Anodic Bonding of Nanochannels

To optimize anodic bonding conditions and nanochannel filter dimensions, nanochannels of different dimensions were patterned across six 6-in silicon wafers and a  $5000 \text{ \AA}$  thermal oxide was grown on each wafer. Blank Pyrex wafers were

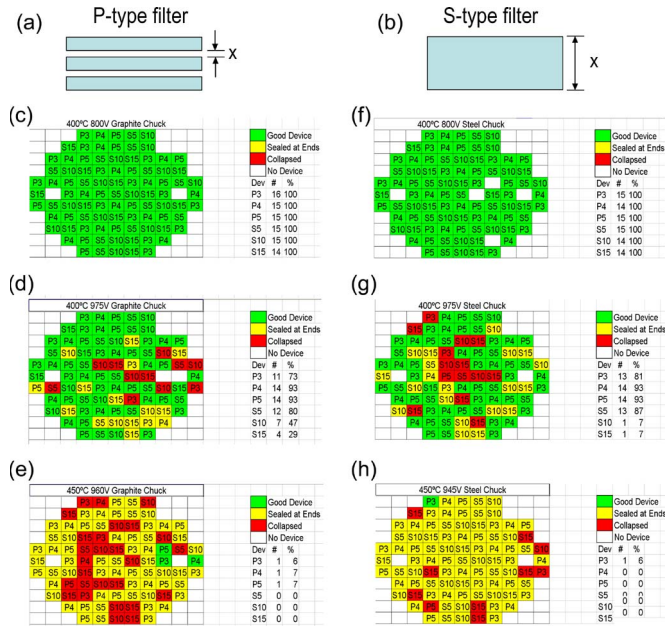


Fig. 8. Results of nanochannel anodic bonding experiments. Nanochannel structures of two types were tested. (a) P-type filters are labeled  $PX$ , where  $X$  refers to the width of pillars between three  $5 \mu\text{m} \times 40 \text{ nm}$  nanochannels. (b) S-type filters are labeled  $SX$ , where  $X$  refers to the width of a single  $40\text{-nm}$ -deep nanochannel. Bonding was performed using either a (c)–(e) graphite chuck or (f)–(h) a steel chuck at the temperatures and voltages indicated in the figure. Following bonding, filters were observed under a microscope with bright-field illumination to determine if (green) nanochannels were intact, (yellow) sealed at the ends, or (red) completely collapsed.

then anodically bonded to the silicon wafers under a variety of conditions. Three wafers were bonded using a graphite chuck and the other three using a steel chuck. For each set of three wafers, one was bonded at  $400^\circ\text{C}$  and  $800 \text{ V}$ , one at  $400^\circ\text{C}$  and  $\sim 1000 \text{ V}$ , and one at  $450^\circ\text{C}$  and  $\sim 1000 \text{ V}$  (due to power supply current limits, the maximum applicable voltage varied somewhat between experiments). After bonding, the wafers were examined under a microscope with bright-field illumination to determine if nanochannels were collapsed, and the results are summarized in Fig. 8. Based on these results, it was determined that the graphite chuck produced the most uniform bond, and that the most extreme bonding conditions that could be employed without significant nanochannel collapse were  $400^\circ\text{C}$  and  $1000 \text{ V}$ . Notably, when these conditions were applied to the same wafer pairs but with ultrasonically drilled holes present in the Pyrex wafer ( $250 \mu\text{m}$  diameter, 910 holes per  $6''$  wafer), millimeter-scale areas of the bond interface were found to be delaminated based on the observation of Newton rings. This delamination was attributed to the presence of the holes and not simply to process variation because the delaminated regions occurred almost exclusively in between access holes, as seen in Fig. 9. Although these trial wafers did not contain functional NC structures, large-scale delamination of this type was also observed in earlier integrated-device processes where access holes were made in the Pyrex lid, and these devices exhibited NC ionic conductivities which were too high to support stable concentration polarization (results not shown). For these reasons, it was necessary to develop a process

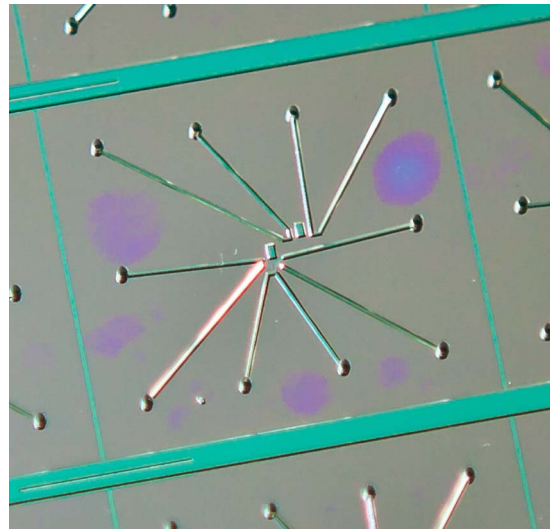


Fig. 9. Photograph of a silicon wafer that is anodically bonded to a Pyrex wafer containing ultrasonically drilled access holes ( $250 \mu\text{m}$  diameter, 910 holes per  $6''$  wafer). Delaminated regions, which appear violet in color, occur almost exclusively in between access holes.

TABLE I  
PARAMETERS USED IN THE MODEL OF STEADY-STATE BINDING OF A SAMPLE PLUG CONTAINING CONCENTRATED LIGANDS TO RECEPTOR-FUNCTIONALIZED SMR SURFACES

Symbol	Definition	Value(s) Simulated
$V$	SMR Volume	$25 \text{ pL}$
$A$	SMR Surface Area	$2 \times 10^{-4} \text{ cm}^2$
$k$	Forward Reaction Rate	$4 \times 10^4 \text{ M}^{-1} \text{ s}^{-1}$
$c_0$	Initial Ligand Concentration	$1 \text{ nM} - 1 \text{ mM}$
$D$	Ligand Diffusivity	$10^{-7} \text{ cm}^2/\text{s}$
$K_D$	Dissociation Constant	$10^{-9} - 10^{-4} \text{ M}$
$R_T$	Receptor Density	$1 \text{ pmol}/\text{cm}^2$

where access holes are made through the SOI stack instead of the Pyrex lid.

### B. Theoretical Detection Limit for Surface Assays

To estimate the detection limit of the integrated system for a surface assay, we consider the dynamic binding of a sample plug containing concentrated ligands to receptor-functionalized SMR surfaces. In this model, the sample has a fixed volume  $V$  and concentration  $c_0$ , which represents the endpoint concentration after preconcentration. The SMR surface receptors have surface density  $R_T$  and are completely unbound at the beginning of the simulation. Ligands have diffusivity  $D$ , and receptor-ligand binding is characterized by a forward reaction rate,  $k$ , and dissociation constant,  $K_D$ . The parameters used in the simulation are summarized in Table I. Since the Damkohler number  $Da = khR_T/D$  is  $6 \times 10^{-2}$  for this system, it is expected to behave in a reaction-limited manner, so that

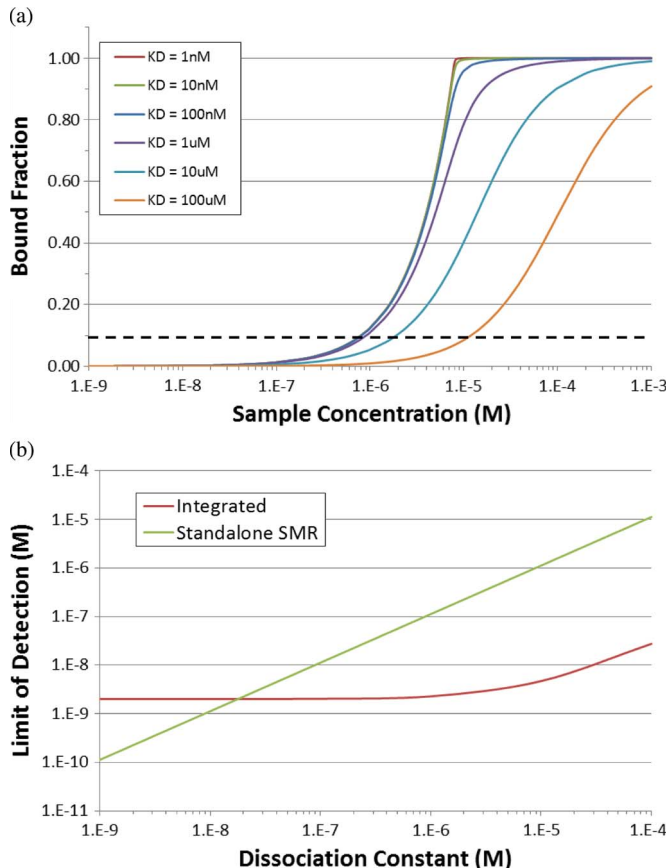


Fig. 10. (a) Simulated bound fraction in equilibrium obtained from (A-2). The dashed line indicates the estimated experimental noise threshold. (b) Dependence on  $K_D$  of the detection limit for the integrated system after 1 h of preconcentration compared with a continuous-flow assay with no preconcentration.

diffusion rapidly equalizes any concentration gradients, and we can consider the concentration independent of space, except in a very small boundary layer near the wall where the reaction occurs. With this assumption, the time dependence of the bound receptor fraction,  $R$  is given by

$$\frac{dR}{dt} = k(c_0 - \phi R_T R)(1 - R) - kK_D R \quad (\text{A-1})$$

where  $\phi$  represents the surface area to volume ratio. In steady state, the solution to (A-1) is

$$R_{equ} = \frac{1}{2\phi R_T} \left( c_0 + K_D + \phi R_T - \sqrt{(c_0 + K_D + \phi R_T)^2 - 4c_0\phi R_T} \right) \quad (\text{A-2})$$

which is plotted in Fig. 10(a) for a range of dissociation constants. A fully ligated surface is expected to cause a shift in resonant frequency of  $\sim 1$  Hz, and based on previous experience with stand-alone SMR systems, a conservative estimate of the minimum resolvable shift is  $\sim 100$  mHz due to baseline drift. Therefore, for the purpose of simulation, the threshold used to define the detection limit is taken to be one tenth of the full-scale signal, as indicated by the dashed line in Fig. 10(a).

The detection limit is determined by dividing the concentration corresponding to the intercept with this threshold by the net preconcentration factor, which was taken to be the maximum factor achievable in one hour,  $10^4$ , divided by the  $\sim 25$ -fold volume mismatch between the concentrated sample and the SMR. This estimate assumes that the concentrated sample diffusively fills the SMR volume before reacting with the surface. In Fig. 10(b), the detection limits of the integrated system is compared with that of a conventional immunoassay in which the ligand continuously flowed through the SMR without preconcentration until equilibrium is reached. It is evident from this plot that the detection limit in the integrated system is much less sensitive to the properties of the probe compared with a conventional immunoassay. This arises from the fact that the equilibrium reached in the integrated system is determined by the finite number of molecules in the sample after preconcentration, and this feature is absent from a conventional immunoassay where convective transport of the ligand is sufficiently large that free ligand depletion can be ignored. Because the sample is finite in the concentrated sample plug, significant depletion of the free ligand concentration can occur as it equilibrates with the surface, and this results in a sharp binding response when the concentration of the sample,  $c_0$ , surpasses the concentration of receptors in the SMR ( $R_T A/V = 8 \mu\text{M}$  in this simulation), as seen in Fig. 10(a). Hence, for probe systems where the dissociation constant is significantly smaller than the receptor concentration, the detection limit of the integrated system assumes a constant value which is approximated by this concentration divided by the total preconcentration factor. Hence, the integrated system is not able to take advantage of highly sensitive probes to achieve a lower detection limit like a conventional assay. The conventional assay's performance exceeds that of the integrated system for dissociation constants below 18 nM. For dissociation constants significantly larger than the receptor concentration, free ligand depletion can be ignored even for the integrated system, and the detection limit approaches that of the conventional assay divided by the preconcentration factor. It is therefore expected that preconcentration using the existing integrated system will produce an improvement in the detection limit of an immunoassay for probe systems having a dissociation constant of at least 18 nM.

## REFERENCES

- [1] Y. C. Wang and J. Han, "Pre-binding dynamic range and sensitivity enhancement for immuno-sensors using nanofluidic preconcentrator," *Lab Chip*, vol. 8, no. 3, pp. 392–394, Mar. 2008.
- [2] Y. C. Wang, A. L. Stevens, and J. Han, "Million-fold preconcentration of proteins and peptides by nanofluidic filter," *Anal. Chem.*, vol. 77, no. 14, pp. 4293–4299, Jul. 2005.
- [3] D. S. Burgi and R. L. Chien, "Optimization in sample stacking for high-performance capillary electrophoresis," *Anal. Chem.*, vol. 63, no. 18, pp. 2042–2047, Sep. 1991.
- [4] R. L. Chien and D. S. Burgi, "Sample stacking of an extremely large injection volume in high-performance capillary electrophoresis," *Anal. Chem.*, vol. 64, no. 9, pp. 1046–1050, May 1992.
- [5] J. Lichtenberg, E. Verpoorte, and N. F. de Rooij, "Sample preconcentration by field amplification stacking for microchip-based capillary electrophoresis," *Electrophoresis*, vol. 22, no. 2, pp. 258–271, Jan. 2001.
- [6] C. X. Zhang and W. Thormann, "Head-column field-amplified sample stacking in binary system capillary electrophoresis: A robust approach providing over 1000-fold sensitivity enhancement," *Anal. Chem.*, vol. 68, no. 15, pp. 2523–2532, Aug. 1996.

- [7] P. Gebauer, Z. Mala, and P. Bocek, "Recent progress in analytical capillary ITP," *Electrophoresis*, vol. 30, no. 1, pp. 29–35, Jan. 2009.
- [8] M. Molina and M. Silva, "Micellar electrokinetic chromatography: Current developments and future," *Electrophoresis*, vol. 23, no. 22/23, pp. 3907–3921, Dec. 2002.
- [9] J. P. Quirino and S. Terabe, "Exceeding 5000-fold concentration of dilute analytes in micellar electrokinetic chromatography," *Science*, vol. 282, no. 5388, pp. 465–468, Oct. 1998.
- [10] J. P. Quirino and S. Terabe, "Approaching a million-fold sensitivity increase in capillary electrophoresis with direct ultraviolet detection: Cation-selective exhaustive injection and sweeping," *Anal. Chem.*, vol. 72, no. 5, pp. 1023–1030, Mar. 2000.
- [11] J. Astorga-Wells, T. Bergman, and H. Jornvall, "Multistep microreactions with proteins using electrocapture technology," *Anal. Chem.*, vol. 76, no. 9, pp. 2425–2429, May 2004.
- [12] J. Astorga-Wells and H. Swerdlow, "Fluidic preconcentrator device for capillary electrophoresis of proteins," *Anal. Chem.*, vol. 75, no. 19, pp. 5207–5212, Oct. 2003.
- [13] Q. G. Wang, B. F. Yue, and M. L. Lee, "Mobility-based selective on-line preconcentration of proteins in capillary electrophoresis by controlling electroosmotic flow," *J. Chromatogr. A*, vol. 1025, no. 1, pp. 139–146, Jan. 2004.
- [14] B. S. Broyles, S. C. Jacobson, and J. M. Ramsey, "Sample filtration, concentration, and separation integrated on microfluidic devices," *Anal. Chem.*, vol. 75, no. 11, pp. 2761–2767, Jun. 2003.
- [15] D. L. Huber, R. P. Manginell, M. A. Samara, B. I. Kim, and B. C. Bunker, "Programmed adsorption and release of proteins in a microfluidic device," *Science*, vol. 301, no. 5631, pp. 352–354, Jul. 2003.
- [16] C. Yu, M. H. Davey, F. Svec, and J. M. J. Fréchet, "Monolithic porous polymer for on-chip solid-phase extraction and preconcentration prepared by photoinitiated *in situ* polymerization within a microfluidic device," *Anal. Chem.*, vol. 73, no. 21, pp. 5088–5096, Nov. 2001.
- [17] J. Khandurina, S. C. Jacobson, L. C. Waters, R. S. Foote, and J. M. Ramsey, "Microfabricated porous membrane structure for sample concentration and electrophoretic analysis," *Anal. Chem.*, vol. 71, no. 9, pp. 1815–1819, May 1999.
- [18] S. Song, A. K. Singh, and B. J. Kirby, "Electrophoretic concentration of proteins at laser-patterned nanoporous membranes in microchips," *Anal. Chem.*, vol. 76, no. 15, pp. 4589–4592, Aug. 2004.
- [19] S. Son, W. H. Grover, T. P. Burg, and S. R. Manalis, "Suspended microchannel resonators for ultra-low volume universal detection," *Anal. Chem.*, vol. 80, no. 12, pp. 4757–4760, Jun. 2008.
- [20] M. G. von Muhlen, N. D. Brault, S. M. Knudsen, S. Jiang, and S. R. Manalis, "Label-free biomarker sensing in undiluted serum with suspended microchannel resonators," *Anal. Chem.*, vol. 82, no. 5, pp. 1905–1910, Mar. 2010.
- [21] T. P. Burg, M. Godin, S. M. Knudsen, W. Shen, G. Carlson, J. S. Foster, K. Babcock, and S. R. Manalis, "Weighing of biomolecules, single cells, and single nanoparticles in fluid," *Nature*, vol. 446, no. 7139, pp. 1066–1069, Apr. 2007.
- [22] A. Höltzel and U. Tallarek, "Ionic conductance of nanopores in microscale analysis systems: Where microfluidics meets nanofluidics," *J. Separation Sci.*, vol. 30, no. 10, pp. 1398–1419, Jul. 2007.
- [23] S. S. Dukhin, "Electrokinetic phenomena of the second kind and their applications," *Adv. Colloid Interface Sci.*, vol. 35, pp. 173–196, Mar. 1991.
- [24] N. A. Mishchuk and P. V. Takhistov, "Electroosmosis of the second kind," *Colloids Surf. A—Physicochemical Eng. Aspects*, vol. 95, no. 2/3, pp. 119–131, Feb. 1995.
- [25] S. J. Kim, L. D. Li, and J. Han, "Amplified electrokinetic response by concentration polarization near nanofluidic channel," *Langmuir*, vol. 25, no. 13, pp. 7759–7765, Jul. 2009.
- [26] S. J. Kim, Y. C. Wang, J. H. Lee, H. Jang, and J. Han, "Concentration polarization and nonlinear electrokinetic flow near a nanofluidic channel," *Phys. Rev. Lett.*, vol. 99, no. 4, p. 044501-1, Jul. 2007.
- [27] F. C. Leinweber and U. Tallarek, "Nonequilibrium electrokinetic effects in beds of ion-permselective particles," *Langmuir*, vol. 20, no. 26, pp. 11637–11648, Dec. 2004.
- [28] T. P. Burg, A. R. Mirza, N. Milovic, C. H. Tsau, G. A. Popescu, J. S. Foster, and S. R. Manalis, "Vacuum-packaged suspended microchannel resonant mass sensor for biomolecular detection," *J. Microelectromech. Syst.*, vol. 15, no. 6, pp. 1466–1476, Dec. 2006.
- [29] T. Raj and W. H. Flygare, "Diffusion studies of bovine serum albumin by quasielastic light scattering," *Biochemistry*, vol. 13, no. 16, pp. 3336–3340, Jul. 1974.



**Philip Dextras** received the B.A.Sc. degree in engineering physics from the University of British Columbia, Vancouver, BC, Canada, in 2002, and the Ph.D. degree in biological engineering from the Massachusetts Institute of Technology, Cambridge, MA, in 2009. His doctoral research involved the development of a MEMS-based instrument for measuring the mass and surface charge of single bacterial cells.

He is currently a Research Fellow in the Department of Applied Chemistry, The University of Tokyo, Tokyo, Japan, where his research is in the area of micro/nanofluidic system integration.

Dr. Dextras is the recipient of a fellowship from the Japan Society for the Promotion of Science in 2010.



**Kristofor R. Payer** received the B.S. degree in chemical engineering from the University of Massachusetts, Amherst, in 2003.

He has worked in the microfabrication field for ten years. He spent four years with Axsun Technologies as an Intern and later as an Associate Engineer and one year with the University of Massachusetts as a Research Assistant. He is currently a Research Specialist with the Microsystems Technology Laboratories, Massachusetts Institute of Technology, Cambridge. His previous research interests include

sorption hysteresis in mesoporous materials, optical MEMS tunable filters, and microfluidic MEMS devices. He is currently researching BioMEMS device fabrication, including the suspended microchannel resonator and microfluidic cell traps.



**Thomas P. Burg** (S'00–M'06) received the Dipl.-Phys. degree in physics from the Swiss Federal Institute of Technology (ETH), Zurich, Switzerland, in 2001, and the Ph.D. degree in electrical engineering and computer science from the Massachusetts Institute of Technology (MIT), Cambridge, in 2005.

From 2005 to 2008, he was a Research Associate in biological engineering at MIT. Since 2009, he has been with the Max Planck Institute for Biophysical Chemistry, Goettingen, Germany, as a Max Planck Research Group Leader. His interests are centered

around the development of biological micro/nano-electromechanical systems for applications in light and electron microscopy, physical (bio)chemistry, and cellular biophysics.



**Wenjiang Shen** received the B.S. and M.S. degrees from the Materials Science and Engineering Department, Tsinghua University, Beijing, China, and the Ph.D. degree from the University of California, Los Angeles, in 2004.

He is currently a Program Manager with Innovative Micro Technology, Inc., Santa Barbara, CA. His research concerns microelectromechanical systems and nanotechnology, including the design and fabrication of micro/nanostructures, system integration, and wafer-level packaging.



**Ying-Chih Wang** received the B.S. degree in mechanical engineering from National Taiwan University, Taipei, Taiwan, in 2000, and the M.S. and Ph.D. degrees in mechanical engineering from the Massachusetts Institute of Technology, Cambridge, in 2004 and 2007, respectively, with thesis research on multidimensional biosample preparation technologies and the nanofluidic biosample preconcentrator.

Since 2009, he has been with RheoSense, Inc., San Ramon, CA, developing high-accuracy microelectromechanical system viscosity measurement platforms for biomedical materials and other soft matters. His postgraduate research focused on developing microfluidic systems for rapid biotoxin analysis and point-of-care medical diagnostics.



**Jongyoon Han** (M'04) was born in Seoul, Korea, in 1969. He received the B.S. and M.S. degrees in physics from Seoul National University, Seoul, in 1992 and 1994, respectively, and the M.S. and Ph.D. degrees in applied physics from Cornell University, Ithaca, NY, in 1998 and 2001, respectively.

He was a Research Scientist at Sandia National Laboratories, Livermore, CA, from 2001 to 2002, before joining the Massachusetts Institute of Technology (MIT), Cambridge, as an Assistant Professor in the Department of Electrical Engineering and Computer Science. Later, he joined the Department of Biological Engineering, MIT, as a Dual Faculty Member, and was promoted to the rank of Associate Professor in 2006. His laboratory has been developing various microfluidic systems for biosample preparation, such as nanofilter protein/deoxyribonucleic acid separation systems, as well as biomolecule concentration devices. More recently, his group has been working on biomechanical cell-sorting devices and novel water-purification systems.

Dr. Han is a member of the American Physical Society, American Chemical Society, and Biomedical Engineering Society. He was the recipient of a National Science Foundation CAREER Award (in 2003) and the Analytical Chemistry Young Innovator Award (in 2009).



**Scott R. Manalis** received the B.S. degree in physics from the University of California, Santa Barbara, and the Ph.D. degree in applied physics from Stanford University, Stanford, CA.

He is currently a Member of the Koch Institute for Integrative Cancer Research and a Professor in the Department of Biological Engineering and the Department of Mechanical Engineering, Massachusetts Institute of Technology, Cambridge. His laboratory uses micro- and nanoscale technologies to develop quantitative and real-time techniques for biomolecular detection and single-cell analysis.

Dr. Manalis was the recipient of the Presidential Early Career Award for Scientists and Engineers from the Department of Defense. He has also been selected by *Technology Review* magazine as one of the 100 innovators under the age of 35 whose work and ideas "will have a deep impact on how we live, work, and think in the century to come."